# Spatially resolved edge currents and guided-wave electronic states in graphene

M. T. Allen, O. Shtanko, I. C. Fulga, A. R. Akhmerov, K. Watanabe, T. Taniguchi, P. Jarillo-Herrero, L. S. Levitov, and A. Yacoby*

*Correspondence to: yacoby@physics.harvard.edu

**Modeling electronic guided modes**

<u>Main results</u>

A realistic model of supercurrent-carrying states in graphene SNS junctions should account for several microscopic effects. This includes, in particular, the details of transport through the NS interfaces, the realistic edge potential profile due to band bending near graphene edge, and the effects of disorder. Since treating all these issues simultaneously and on equal footing may be challenging, we use a simplified model. First, we completely ignore the effects of induced superconductivity, focusing on the normal metallic state of pristine graphene. Second, we consider a clean system and account for disorder scattering perturbatively at the end. Third, since all the states in a clean system, being delocalized, are capable of carrying supercurrent, we resort to evaluating the density of states (DOS) taking it to reflect on the current-carrying capacity of the system. Naturally, such an approach should be used with caution for disordered systems in which some states are localized, and therefore can contribute to DOS but not to supercurrent. However, since the states in a clean system are of a plane wave character, contributing to current with the weights given by their occupancies and all possessing a roughly similar current-carrying capacity, we adopt the DOS-based approximation on the merit of its simplicity.

Below we focus on the two cases of interest: the monolayer graphene (MLG) and bilayer graphene (BLG). States in MLG are described by the massless Dirac Hamiltonian

$$
(1) \qquad H_0 = v \begin{pmatrix} 0 & p_x - ip_y \\ p_x + ip_y & 0 \end{pmatrix} = v\sigma_1 p_x + v\sigma_2 p_y
$$

with $v \approx 10^6$ m/s the carrier velocity and $\sigma_1$, $\sigma_2$ the pseudospin Pauli matrices. States in BLG are described by the Hamiltonian

$$
(2) \qquad H_0 = \frac{1}{2m^*} \begin{pmatrix} 0 & (p_x - ip_y)^2 \\ (p_x + ip_y)^2 & 0 \end{pmatrix} = \frac{1}{2m^*}\left\{ \sigma_1(p_x^2 - p_y^2) + 2\sigma_2 p_x p_y \right\}
$$

with the band mass value $m^* = 0.028\, m_e$.

As stated above, we use spatially resolved DOS as a measure of current-carrying capacity of the system. We analyze the quantity

$$
(3) \qquad N(\mu, \mathbf{r}) = \frac{dn(\mathbf{r})}{d\mu}, \quad n(\mathbf{r}) = \langle \psi^\dagger(\mathbf{r})\psi(\mathbf{r}) \rangle,
$$

where $n$ is the total carrier density and $\mu$ is the chemical potential. Below we evaluate DOS as a function of position and energy, focusing on the characteristic features due to the guided modes.

Our analysis of the spatial dependence of DOS and other related quantities is facilitated by the following observations. First, as discussed in the main text, the problem of guided states on a half-plane $x > x_0$ near the edge $x = x_0$ in MLG can be mapped onto a similar problem on a full plane by accounting for the states in valleys $K$ and $K'$ mixing at the edge. This mapping is particularly transparent for the armchair edge, where the boundary condition for the spinor wavefunctions in the two valleys is simply $\psi_K + \psi_{K'} = 0$. In this case, one can see that the two-valley half-plane problem is mathematically equivalent to the problem posed on a full plane for particles in just one valley, provided the line potential for the latter problem is taken to be a sum of the original edge potential and its mirror-reflected double, $V(x > x_0) \rightarrow V(|x - x_0|)$.

Second, the states with the wavelengths larger than the edge potential width can be described by treating the potential in a delta function approximation. In that, a realistic microscopic potential $V(x)$ is replaced by a delta-function pseudopotential

$$(4) \qquad \tilde{V}(x) = \hbar u \delta(x - x_0), \quad u = \frac{1}{\hbar} \int V(x') dx'$$

where $x_0$ is the edge position. Here we parameterized the effective potential strength by the quantity $u$ which has the dimension of velocity. A system of width $w$ with two parallel edges positioned at $x_0 = \pm w/2$ can therefore be described by a Hamiltonian in the full plane $-\infty < x < \infty$, $-\infty < y < \infty$:

$$(5) \qquad H = H_0 + \hbar u \delta(x + w/2) + \hbar u \delta(x - w/2),$$

where $H_0$ is the $2 \times 2$ Dirac Hamiltonian for carriers with one spin/valley projection in MLG or BLG, see Eqs.(1),(2).

Lastly, taking into account that for for relevant densities $n \sim 10^{11}$ cm$^{-2}$ typical electronic wavelength values $\lambda \sim n^{-1/2} \approx 50$ nm are much smaller than the distance between edges $w = 800 - 1200$ nm, we can represent DOS as a sum of partial contributions

$$(6) \qquad N(\mu, x) = N_0(\mu) + N_1(\mu, x - w/2) + N_1(\mu, x + w/2).$$

Here $N_0(\mu)$ is the DOS of a uniform infinite system with fixed spin/valley projection,

$$(7) \qquad N_0(\mu) = \frac{|\mu|}{2\pi\hbar^2 v^2} \text{ (MLG)}, \qquad N_0(\mu) = \frac{m^*}{2\pi\hbar^2} \text{ (BLG)}$$

and $N_1(\mu, x \pm w/2)$ are the contributions to DOS from a pair of delta-function line potentials placed at $x = \pm w/2$.

Below we derive an exact expression for DOS perturbed by a delta function. For MLG we find

$$(8) \qquad N_1(\varepsilon, x) = \frac{4u}{\pi\hbar^2} \text{Im} \int \frac{dp}{2\pi} \frac{p^2 e^{-2\kappa_{\varepsilon,p}|x|/\hbar}}{\kappa_{\varepsilon,p}\left[4\varepsilon u + (4v^2 - u^2)\kappa_{\varepsilon,p}\right]} \qquad \text{(MLG)}$$

where $\kappa_{\varepsilon,p} = \sqrt{p^2 - (\varepsilon/v)^2}$. For BLG we find

$$(9)$$
$$N_1(\varepsilon, x) = -\frac{2}{\pi\hbar^2 u} \text{Im} \int \frac{dp}{2\pi} \frac{[1 + F_0(0)][F_0^2(x) + F_1^2(x) + F_2^2(x)] - 2F_1(0)F_0(x)F_1(x)}{[1 + F_0(0)]^2 - F_1^2(0)} \qquad \text{(BLG)}$$

where we introduced the notation

(10)
$$F_0(x) = \frac{m^*u}{2}\left[\frac{1}{\kappa_{\varepsilon,p}^-}e^{-\kappa_{\varepsilon,p}^-|x|} - \frac{1}{\kappa_{\varepsilon,p}^+}e^{-\kappa_{\varepsilon,p}^+|x|}\right]$$

(11)
$$F_1(x) = \frac{m^*u}{2}\left[\frac{1}{\kappa_{\varepsilon,p}^-}\left(1 - \frac{p^2}{m^*\varepsilon}\right)e^{-\kappa_{\varepsilon,p}^-|x|} + \frac{1}{\kappa_{\varepsilon,p}^+}\left(1 + \frac{p^2}{m^*\varepsilon}\right)e^{-\kappa_{\varepsilon,p}^+|x|}\right]$$

(12)
$$F_2(x) = -\frac{pu}{2\varepsilon}\left(e^{-\kappa_{\varepsilon,p}^-|x|} - e^{-\kappa_{\varepsilon,p}^+|x|}\right)$$

where $\kappa_{\varepsilon,p}^{\pm} = \sqrt{p^2 \pm 2m^*\varepsilon}$.

In the expressions given in Eq.(8) and Eq.(9) the energy $\varepsilon$ is taken to have an infinitesimal positive imaginary part, which is essential for handling the poles in the denominators due to the guided modes. After evaluating the integral, $\varepsilon$ must be replaced by the chemical potential, $\varepsilon = \mu$. The spatial dependence of DOS in MLG described by Eq.(8) is shown in Fig. S1.

In our model, which is essentially non-interacting, the effects of screening can be included in a heuristic way by treating the potential strength in Eq.(5) as a function of carrier density parameterized by the chemical potential $\mu$. We use a simple model which captures the overall behavior seen in the data

(13)
$$u \to u'(\mu) = \frac{u}{1 + (|\mu|/\mu_0)^\alpha}$$

where the parameter $\mu_0$ depends on microscopic details. Comparing to the data indicates that a reasonably good fit can be achieved for $\alpha \approx 2$.

The results for MLG, of the form given in Eq. (6), are presented in Fig. 1c of the main text. The spatially resolved density of states is obtained for carrier densities $n = 0.05 \cdot 10^{11}\text{cm}^{-2}$ (red curve) and $n = 2.5 \cdot 10^{11}\text{cm}^{-2}$ (blue curve), where $n$ accounts for the spin and valley degeneracy. Potential strength used is $\hbar u = -1.5\,\hbar v \approx 1$ eV·nm, the screening parameter value is $\mu_0 = 0.2\sqrt{\pi\hbar^2 v^2 n_0} \approx 7$ meV, with $n_0 = 10^{11}\text{cm}^{-2}$ the corresponding carrier density.

A similar approach was used to model the density profile in BLG, with a pair of line delta functions mimicking the graphene edge potential. The resulting spatially resolved DOS in BLG, of the form given in Eq.(6) with $N_1(\varepsilon, x)$ defined in Eq.(9), is shown in Fig. 4b of the main text. The delta-function potential strength was parameterized in the same way as for MLG. The curves in Fig. 4b were obtained using the best-fit value $\hbar u = 0.7$ eV·nm and assuming no screening.

Microscopic derivation

To obtain Eq. (8) and Eq. (9) we consider long-wavelength modes for a line potential positioned at $x = 0$. This problem is described by the Hamiltonian $H = H_0 + V(x)$ with $V(x) = \hbar u \delta(x)$. Here we construct the Greens function which takes the full account of scattering by the potential $V(x)$. The discrete spectrum of the system, arising due to guided modes, can be conveniently expressed through the poles of the electron Greens function. The Greens function, in this case, can be evaluated using Dysons's equation and the T-matrix representation:

(14)
$$G = G_0 + G_0VG_0 + G_0VG_0VG_0 + \cdots = G_0 + G_0TG_0$$

where $G_0 = (i\varepsilon - H_0)^{-1}$.

Naively, Dyson's equation for the T-matrix can be solved in an explicit way as

$$(15) \qquad T(\varepsilon, p_y) = \hbar u \left(1 - \hbar u \int \frac{dp_x}{2\pi\hbar} G_0(\varepsilon, \mathbf{p})\right)^{-1}$$

In our problem, however, such a solution potentially misses the effects of the electron wavefunction phase variation in space near the delta-function potential. Indeed, the result in Eq.(15) can be seen to rely on the assumption of the wavefunction continuity in the vicinity of the delta-function. However, the property of wavefunction continuity holds for BLG but does not hold for MLG where the wave-function phase experiences a jump across the delta-function (see discussion in the main text). The correct expression for the T-matrix for the MLG case, which is more complicated than that in Eq.(15), can be constructed by performing a suitable gauge transformation (to be discussed elsewhere). This analysis also indicates that despite the discontinuity pitfalls Eq.(15) provides a reasonable approximation at not too large coupling strength values $u$. We will therefore use Eq.(15) on the merit of its simplicity to evaluate DOS at the weak-to-moderate coupling strengths. For that Eq.(15) has to be combined with the general expression for spatially resolved DOS

$$(16) \qquad N(\varepsilon, \mathbf{r}) = -\frac{1}{\pi} \operatorname{Im} \operatorname{Tr} G(\varepsilon, \mathbf{r}, \mathbf{r}')_{\mathbf{r}=\mathbf{r}'},$$

where the energy variable is analytically continued from positive imaginary values to real values via $i\varepsilon \rightarrow \varepsilon + i0$ with the trace taken over pseudospin variables. The results of this calculation for the MLG and BLG systems are presented below.

### Microscopic derivation: MLG case

Evaluating the integral in Eq.(15) gives

$$(17) \qquad T(\varepsilon, p_y) = \hbar u \left(1 + \frac{u}{2v} \left(i\tilde{\varepsilon} + \sigma_1 \tilde{p}\right)\right)^{-1}$$

where we defined

$$(18) \qquad \tilde{\varepsilon} = \frac{\varepsilon}{\sqrt{\varepsilon^2 + v^2 p_y^2}} \qquad \tilde{p} = \frac{v p_y}{\sqrt{\varepsilon^2 + v^2 p_y^2}}$$

Here $\varepsilon$ is the Euclidean (Matsubara) frequency. Performing the analytic continuation $i\varepsilon \rightarrow \varepsilon + i0$ we find the T-matrix poles

$$(19) \qquad \varepsilon = \pm \tilde{v}|p_y|, \quad \tilde{v} = v \frac{4v^2 - u^2}{4v^2 + u^2}$$

where the sign is given by $\pm = \operatorname{sign} u$. Eq.(19) describes the guided mode dispersion. Since $|\tilde{v}| < v$, the energies $\varepsilon = \pm\tilde{v}|p_y|$ are positioned, for each $p_y$ value, outside the Dirac continuum of the bulk states. This expression behaves in a qualitatively similar way to the exact dispersion derived in the main text, Eq. (1) (see Fig.1a of the main text). The guided modes described by Eq.(19) are quasi-1D states that propagate as plane waves in the $y$ direction along the $x = 0$ line and decay exponentially as evanescent waves in the transverse direction.

To proceed with our calculation of spatially resolved DOS, we need Greens function evaluated in a mixed position-momentum representation

$$(20) \qquad G_0(\varepsilon, p_y, x) = \int \frac{dp_x}{2\pi\hbar} e^{ip_x x} G_0(\varepsilon, \mathbf{p}) = \frac{-i\tilde{\varepsilon} - \sigma_2 \tilde{p} - i\sigma_1 \operatorname{sign}(x)}{2\hbar v} \exp\left(-\kappa(i\varepsilon)|x|/\hbar\right)$$

where $\kappa(i\varepsilon) = \sqrt{(\varepsilon/v)^2 + p_y^2}$.

The trace of an equal-point Greens function in Eq.(16) then could be evaluated from Eq.(14) with the help of Eq.(17):

$$(21) \qquad \mathrm{Tr}\, G(\varepsilon, x' = x) = \sum_{p_y} \left( \frac{\tilde{\varepsilon}}{i\hbar v} + \frac{4u\tilde{p}^2 e^{-2\kappa|x|/\hbar}}{\hbar \left[ (2v + iu\tilde{\varepsilon})^2 - u^2\tilde{p}^2 \right]} \right)$$

where the two terms represent contributions of $G_0$ and $G_0 T G_0$, repectively.

We start with considering the first term of (21). Introducing a UV cutoff $p_0 = \varepsilon_0/v$ we evaluate the sum over $p_y$ as

$$(22) \qquad \int_{-p_0}^{p_0} \frac{dp_y}{2\pi\hbar} \frac{\varepsilon}{\sqrt{\varepsilon^2 + v^2 p_y^2}} = \frac{\varepsilon}{\pi\hbar v} \ln \frac{\varepsilon_0}{\varepsilon}.$$

Performing analytic continuation $i\varepsilon \to \delta - i\varepsilon$, we arrive at

$$(23) \qquad N_0(\varepsilon) = -\frac{\varepsilon}{\pi^2\hbar^2 v^2} \mathrm{Im}\, \ln \frac{\varepsilon_0}{\delta - i\varepsilon}$$

where $\delta = +0$. Taking the imaginary part, we obtain the expression in Eq.(7).

Next, we evaluate the second term in Eq.(21). Performing the same analytic continuation, we arrive at the result in Eq.(8). The expression in Eq.(8) can be conveniently analyzed by dividing the integral into two parts, taken over the domains $|p_y| > |\varepsilon|/\hbar v$ and $|p_y| < |\varepsilon|/\hbar v$, respectively. The latter contribution is particularly simple because it is governed by the pole (19) and can be easily evaluated as an integral of a delta function, giving

$$(24) \qquad N_{\mathrm{g.w.}}(\varepsilon, x) = \frac{2u|\varepsilon|}{\hbar^2\tilde{v}(4v^2 - u^2)} e^{-2\sqrt{(v/\tilde{v})^2 - 1}|x||\varepsilon|/\hbar v}$$

This contribution is solely due to the guided mode. As illustrated in the Fig S1, this term dominates the peak structure in DOS for guided waves. The contribution of the region $|p_y| > |\varepsilon|/\hbar v$ describes the enhancement of DOS dues to the states in the continuum being pulled on the delta-function potential. This contribution is evaluated numerically.

We used the full expression in Eq.(8) to produce the spatially resolved DOS curves shown in Fig.1c of the main text. In that, we accounted for screening, as described in Eq.(13). Because of screening, the peak structure is more prominent at low chemical potential, and is suppressed relatively to the bulk DOS at high chemical potential values.

Microscopic derivation: BLG case

Following the same procedure as above, we derive the free electron Greens function for BLG in a mixed position-momentum representation:

$$(25) \qquad G_0(\varepsilon, p_y, x) = \int \frac{dp_x}{2\pi\hbar} e^{ip_x x} G_0(\varepsilon, \mathbf{p}) = -\frac{1}{\hbar u} \Big( F_0(x) + \sigma_1 F_1(x) + i\sigma_2 F_2(x)\mathrm{sign}(x) \Big)$$

where we used the quantities defined in Eqs. (10)-(12). The dispersion relation can then be obtained from the T-matrix:

$$(26) \qquad T(\varepsilon, p_y) = \hbar u \Big( 1 - \hbar u G_0(\varepsilon, p_y, x)\big|_{x=0} \Big)^{-1}$$

Solving for the poles of this $2 \times 2$ T-matrix, we obtain two independent equations describing mode dispersion

$$(27) \qquad \varepsilon(p) = \frac{u}{2}\left(\kappa_{\varepsilon,p}^{+} - \frac{p^2}{\kappa_{\varepsilon,p}^{-}}\right), \qquad \varepsilon(p) = \frac{u}{2}\left(\kappa_{\varepsilon,p}^{-} - \frac{p^2}{\kappa_{\varepsilon,p}^{+}}\right)$$

where $\kappa_{\varepsilon,p}^{\pm} = \sqrt{p^2 \pm 2m^*\varepsilon(p)}$. These equations have be easily solved numerically, giving two independent guided modes.

The resulting mode spectrum is more complicated than in the MLG case, Eq.(19). For energies $\varepsilon \leq \varepsilon' = m^*u^2/4$ two modes exist, whereas for higher energies only one mode exists. The latter features dispersion with the large-$p_y$ asymptotic of the form

$$(28) \qquad \varepsilon(p_y) \approx -\operatorname{sign} u\left(\frac{p_y^2}{2m^*} - \frac{m^*u^2}{4}\right) \qquad |p_y| \gg m^*|u|$$

For both modes the dispersion relation is such that the mode frequencies lie outside the continuum spectrum of BLG bulk (see Fig.1b of the main text). This property ensures 1D confinement.

### The effect of disorder

In the presence of disorder scattering, guided modes acquire a finite lifetime. This is described by a complex dispersion frequency

$$(29) \qquad \varepsilon = \tilde{v}|p_y| - i\gamma/2$$

where the imaginary part can be expressed through the inverse lifetime, $\gamma = 1/\tau$.

Here we estimate the effect of disorder scattering assuming that it occurs predominantly at the graphene edge. We model the effect of edge roughness by a fluctuating confining potential strength, for simplicity treating the fluctuations as a gaussian white noise:

$$(30) \qquad V(x,y) = \hbar\Big(u + \delta u(y)\Big)\delta(x), \quad \Big\langle \delta u(y)\delta u(y')\Big\rangle = \frac{\alpha}{\hbar^2}\delta(y - y').$$

Writing the Greens function as a series expansion in the potential $V + \delta V$, Eq.(30), we have

$$(31) \qquad G = G_0 + G_0(V + \delta V)G_0 + G_0(V + \delta V)G_0(V + \delta V)G_0 + ...$$

In averaging the Greens function over disorder, we employ the gaussian noise model in which we only need to account for the pair correlators $\langle \delta u(y)\delta u(y')\rangle$. In a non-crossing approximation, we express the disorder-averaged Greens function through a suitable self-energy

$$(32) \qquad \langle G \rangle = G_0 + G_0(V + \Sigma)G_0 + G_0(V + \Sigma)G_0(V + \Sigma)G_0 + ...$$

where

$$(33) \qquad \Sigma(\varepsilon) = \alpha \int \frac{dp_x}{2\pi\hbar} G(\varepsilon, p_y, x, x')_{x=x'=0}$$

The quantity (33) is complex-valued, with the imaginary part expressed through the density of states $N(\varepsilon)$ at $x = 0$ as

$$(34) \qquad \operatorname{Im}\operatorname{Tr}\Sigma(\varepsilon) = -\pi\alpha N(\varepsilon)_{x=0}.$$

The disorder scattering rate for the guided waves in MLG can now be found from the dispersion relation obtained from the T-matrix pole, Eg(15), which is corrected by the presence of $\Sigma$ as follows

$$(35) \qquad 1 + (\hbar u + \Sigma(i\varepsilon))\frac{i\tilde{\varepsilon} + \sigma_1\tilde{p}}{2\hbar v} = 0.$$

Here we continue to use the Euclidean (Matsubara) frequency notation, as in Eqs.(15), (17).

Since the density of states scales linearly with energy, $N(\varepsilon) \sim |\varepsilon|$ (see Eqs.(24),(7)), we can solve Eq.(35) in the long-wavelength limit treating $\Sigma(i\varepsilon)$ as a perturbation. Writing $\varepsilon = \varepsilon_0(p_y) + \delta\varepsilon$, where $\varepsilon_0 = \tilde{v}|p_y|$ is a solution for $\Sigma = 0$, we linearize in $\delta\varepsilon$ to obtain

$$(36) \qquad \delta\varepsilon = -\frac{1}{\hbar u}\Big(1 - \frac{\tilde{v}^2}{v^2}\Big)\Sigma(i\varepsilon_0)|p_y|v$$

where $\tilde{v}$ is given by Eq.(19). After analytic continuation, we obtain dispersion relation in the form (29) with

$$(37) \qquad \gamma(p_y) = \frac{\pi\alpha}{\hbar|u|}\Big(1 - \frac{\tilde{v}^2}{v^2}\Big)|p_y|vN\big(\tilde{v}|p_y|\big)_{x=0}$$

Accounting for the linear scaling $N(\varepsilon) \sim |\varepsilon|$, we find that the damping rate scales as $p_y^2$,

$$(38) \qquad \gamma(p_y) = \frac{2\pi\alpha p_y^2}{\hbar^3(4v^2 - u^2)}\Big(1 - \frac{\tilde{v}^2}{v^2}\Big)$$

(we approximated the density of states by the expression in Eq.(24) which dominates near the line potential). The mean free path, defined by $l = \tilde{v}\tau$ with $\tau = \hbar/\gamma$, can now be related to the guided mode wavelength $\lambda$ as

$$(39) \qquad l = \frac{\lambda^2}{\xi}, \quad \xi = \frac{8\pi^3\alpha}{\hbar^2v^2}\frac{1 - \tilde{v}^2/v^2}{4 - u^2/v^2}.$$

For an edge which is rough on the atomic scale we expect the values $\xi$ on the order of lattice constant. The mean free path given by Eq.(39) grows rapidly with wavelength. Physically, the quadratic scaling $l \sim \lambda^2$ in Eq.(39) originates from the confinement becoming weaker at small $\varepsilon$, which allows the mode to diffract around disorder. This is in a direct analogy with the weakly guiding fiber designs for optical waves, where weak confinement is employed to achieve exceptionally long mean free paths.

Similar estimates hold for the BLG case. Indeed, the property of waves to diffract around disorder of the characteristic scale smaller than the wavelength is completely general, being valid for waves of any nature, electronic or else. Since the relation between carrier density and wavelength is the same for MLG and BLG, experimental densities translate to the wavelength values similar to those used above, $\lambda \sim 50$ nm. As in the MLG case, scattering by a short-range scatterers localized at the edge becomes inefficient at small $\varepsilon$, leading to large mean free path values.

**Materials and Methods**

Josephson junctions: Device overview

We analyze five graphene Josephson junctions on hBN with widths ranging from $W = 800 - 1200$ nm and lengths ranging from $L = 250 - 350$ nm (see Fig. 1d of the main text for a labeled device schematic). Listed in Table S1 are details on individual sample geometries. The small $L/W$ aspect ratios place these devices are in the narrow junction limit, where the the critical current $I_c$ can be approximated as a phase dependent summation over many parallel 1D current channels (Eq. (1) in the main text). Electrical measurements are conducted using standard Lockin techniques in a Leiden Cryogenics Model Minikelvin 126-TOF dilution refrigerator with a base temperature of 10 mK, well below the critical temperature of Al.

Using a dry transfer method, graphene/hBN stacks are sequentially deposited on a 300 nm thermally grown $SiO_2$ layer, which covers a doped silicon substrate functioning as a global back gate. Graphene flakes are etched to the desired geometry using a 950 PMMA A4 polymer mask ($\sim 200$ nm thick; spun at 4000 rpm) followed by an RIE O2 plasma etch. Titanium/aluminum (Ti/Al) superconducting electrodes are defined on selected flakes using electron beam (ebeam) lithography on a 950 PMMA A4 resist mask, followed by thermal evaporation and liftoff in acetone. For the titanium adhesion layer, we evaporate 10 nm at a rate of 0.3 Angstrom/s. This is followed by an evaporation of a 70 nm aluminum layer at a rate of 0.5 Angstrom/s at pressures in the low to mid $10^{-7}$ Torr range. For dual-gated bilayers, suspended top gates are fabricated using a standard PMMA/MMA/PMMA trilayer resist method which leaves a 200 nm air gap between the top gate and graphene. After using ebeam lithography to define the gates, which employs position-dependent dosage, Cr/Au (3/425 nm) gates are deposited using thermal evaporation and liftoff in acetone. To remove processing residues and enhance quality, devices were current annealed in vacuum at dilution refrigerator temperatures. We note that edge currents were detected both in current-annealed and intrinsically high quality non-annealed devices; typically the appearance of edge currents coincided with the occurrence of Fabry-Perot interference in the ballistic transport regime. All five graphene Josephson junctions exhibit similar transport behavior. Additional data sets are provided in the Supplementary Figures.

Fourier method for extraction of supercurrent density distribution

In a magnetic field $B$, the critical current $I_c(B)$ through a Josephson junction equals the magnitude of the complex Fourier transform of the current density distribution $J(x)$:

$$(40) \qquad I_c(B) = |\mathcal{I}_c(B)| = \left| \int_{-\infty}^{\infty} J(x) \exp(2\pi i (L + l_{Al}) B x / \Phi_0) dx \right|$$

where $x$ is the dimension along the width of the superconducting contacts (labeled in Fig. 1d of the main text), $L$ is the distance between contacts, $l_{Al}$ is the magnetic penetration length (due to a finite London penetration depth in the superconductor and flux focusing), and $\Phi_0 = h/2e$ is the flux quantum. Relevant in the narrow junction limit where current is only a function of one coordinate, Eq. (40) provides a simple and concise description of our system. We employ Fourier techniques introduced by Dynes and Fulton to extract the real space current density distribution from the magnetic interference pattern $I_c(B)$. By expressing the current density as $J(x) = J_s(x) + J_a(x)$, where $J_s(x)$ and $J_a(x)$ are the symmetric and antisymmetric components, the complex critical current can

be rewritten as:

$$(41) \quad \mathcal{I}_c(B) = \int_{-\infty}^{\infty} J_s(x) \cos(2\pi(L+l_{Al})Bx/\Phi_0)dx + i \int_{-\infty}^{\infty} J_a(x) \sin(2\pi(L+l_{Al})Bx/\Phi_0)dx$$

We calculate symmetric component of distribution, the relevant quantity for analyzing edge versus bulk behavior, as the antisymmetric component goes to zero in the middle of the sample. For symmetric solutions, $\mathcal{I}_c(B)$ is purely real. To reconstruct $\mathcal{I}_c(B)$ from the measured critical current, the sign of $I_c(B)$ is reversed for alternating lobes of the Fraunhofer interference patterns. The extracted supercurrent distribution is expressed as an inverse Fourier transform:

$$(42) \quad J_s(x) \approx \int_{-\infty}^{\infty} \mathcal{I}_c(B) \exp(2\pi i(L+l_{Al})Bx/\Phi_0)dB$$

Because $I_c(B)$ is only nonzero over a rectangular window dictated by the finite scan range $B_{\min} < B < B_{\max}$, distribution extracted numerically is given by the convolution of $J(x)$ with the sinc function. To reduce artifacts due the convolution, we employ a raised cosine filter to taper the window at the endpoints of the scan. Explicitly,

$$(43) \quad J_s(x) \approx \int_{B_{\min}}^{B_{\max}} \mathcal{I}_c(B) \cos^n(\pi B/2L_B) \exp(2\pi i(L+l_{Al})Bx/\Phi_0)dB$$

where $n = 0.5 - 1$ and $L_B = (B_{\max} - B_{\min})/2$ is the magnetic field range of the scan.

While the presence of magnetic vortices can provide a different origin for anomalous Fraunhofer patterns (Ref. (22) in the main text), this physics does not apply to our experiment because the width of our devices is small compared to length scales relevant for that phenomenon. Furthermore, if magnetic vortices were the origin of the anomalous Fraunhofer patterns, they should equally affect response at all carrier densities for the same range of flux. The fact that anomalous patterns only arise at densities near charge neutrality further rules out magnetic vortices as a possible origin.

Gaussian fits to extract edge state widths

To extract a length scale for the width of the edge currents near the Dirac point, we fit the experimental supercurrent density distribution $J_c(x)$ to the Gaussian function

$$(44) \quad J_c^G(x) = b \left( \exp\left( \frac{-(x-a)^2}{c} \right) + \exp\left( \frac{-(x+a)^2}{c} \right) \right)$$

where $a$ determines the spatial peak offset, $b$ determines peak height, and $c$ determines peak width. For the data in Fig. 1h of the main text, the fit parameters are $a = 0.515$, $b = 8.8$, and $c = 0.017$. The effective edge current width, given by the Gaussian full width at half maximum $x_{FWHM} = 2\sqrt{c \cdot \ln 2}$, is 220 nm.

Edge versus bulk amplitudes

To more quantitatively assess the evolution of edge and bulk currents with electronic carrier density $n$, we plot line cuts of the individual contributions (see Fig. 2f and 3b of the main text). These are given by:

$$(45) \quad J_c^{edge}(n) = \sum_{x_i=-x_W}^{-x_W+\varepsilon_1} \frac{J_c(x_i, n)}{N_1} \quad \text{and} \quad J_c^{bulk}(n) = \sum_{x_i=-\varepsilon_2}^{\varepsilon_2} \frac{J_c(x_i, n)}{N_2}$$

for a graphene flake whose full width spans from $-x_W$ to $x_W$. $J_c^{edge}(n)$ is the spatially averaged current amplitude over a small window of width $\varepsilon_1$ from the edge of the flake. Similarly, $J_c^{bulk}(n)$ is the spatially averaged current amplitude over a strip of width $2\varepsilon_2$ around the center of the flake. $N_1 = \varepsilon_1/x_{step}$ and $N_2 = \varepsilon_2/x_{step}$, where $x_{step}$ is the distance between data points (determined by the magnetic field range of the scan). For example, for the plots in Fig. 2f of the main text, $x_W = 405$ nm, $\varepsilon_1 = 29$ nm, and $\varepsilon_2 = 87$ nm.

Based on the edge versus bulk current profiles, one may infer whether edge doping is the dominant cause of edge currents in our devices. In the presence of edge doping, the edge versus bulk contributions should be reversed for opposite polarities of bulk carriers (for example, edge dominated behavior at high densities on the electron side and bulk dominated behavior at high densities on the hole side), which is not consistent with the data. Bulk-dominated or flat distributions appear at both high electron and hole doping fairly consistently. As a second test, one can track the edge versus bulk contributions through the Dirac point to detect an offset in gate voltage between the charge neutrality point at the edge versus in the bulk. We did not detect positional density offset substantial enough to account for the large edge currents in these devices (Fig. 2f of the main text).

### Bayesian method for extraction of supercurrent density distribution

The critical current as a function of the magnetic field, $I_c(B)$, is related to the current density through the junction, $J_c(x)$, as

$$
(46) \qquad I_c(B) = \int_{-\frac{W}{2}}^{\frac{W}{2}} dx\, J_c(x) \exp\left(2\pi i x L B/\Phi_0\right),
$$

with $L$ and $W$ the length and width of the junction, and $\Phi_0 = h/2e$ the superconducting flux quantum.

In the measured $|I_c(B)|$ all information about its complex phase is lost, making the problem of determining the current density not have a unique solution. Using the method of Dynes and Fulton (DF), a unique solution can be found under the assumption of a symmetric current distribution, $J_c(x) = J_c(-x)$. In practice however, disorder and inhomogeneities in the junction will lead to asymmetric current densities. Additionally, since experiments are performed over a finite range of magnetic fields, there is a cutoff in the current density resolution. Neither this finite resolution, nor experimental uncertainties are taken into account in the DF method, meaning it can only provide a qualitative estimate of $J_c(x)$.

To gain a more quantitative understanding, we instead ask what is the distribution of $J_c(x)$ which produces the same critical current $I_c(B)$. We answer this question by performing Bayesian inference to obtain the posterior distribution of the current density, given the measured critical current. In our case, Bayes' rule reads:

$$
(47) \qquad \mathcal{H}P\big(J_c; |I_c|\big) = \frac{\mathcal{H}P\big(|I_c|; J_c\big)\,\mathcal{H}P\big(J_c\big)}{\mathcal{H}P\big(|I_c|\big)}.
$$

Here, $\mathcal{H}P\big(J_c; |I_c|\big)$ is the posterior distribution of the current density, the quantity we want to calculate, while $\mathcal{H}P\big(J_c\big)$ is its prior distribution. The likelihood function $\mathcal{H}P\big(|I_c|; J_c\big)$ indicates the compatibility of the measured critical current with a given current density:

$$(48) \qquad \mathcal{H}P\big(|I_c|; J_c\big) = \exp\left[-\frac{(|I_c| - |I_c^f|)^2}{2\varepsilon^2}\right],$$

where $I_c^f$ is the current obtained from $J_c$ by using Eq. (46), $I_c$ is the measured current, and $\varepsilon$ is the measurement error. The factor $\mathcal{H}P\big(|I_c|\big)$ is the same for all current densities, meaning it does not enter into determining their relative probabilities.

The experimental current profiles are extracted from scans of the differential resistance as a function of DC current bias and magnetic field, $dV/dI(I_{\mathrm{DC}}, B)$. Within the same scan, for some field values $dV/dI$ has a clear maximum, while for others it monotonically increases towards its normal state value. We extract the critical current as the value $I_{\mathrm{DC}}$ at which the differential resistance is $x \times \max dV/dI$, choosing a value of $x \lesssim 1$. This selects points close to the maxima at field values where they are well defined, and points close to where the differential resistance reaches its normal state value otherwise. The uncertainty is obtained in the same fashion, by choosing a slightly smaller cutoff.

We maximize the likelihood function using a Monte Carlo sampling algorithm.[1] To get a large resolution of the current density without a significant increase in the dimensionality of the sampling space, we expand $J_c(x)$ as

$$(49) \qquad J_c(x) = \sum_{n=0}^{N} A_n \cos(2\pi n x/L)$$

and enforce $J_c(x) > 0$ for all $x$. The $A_n$ coefficients determine the shape of the distribution, which in Eq. (49) is assumed to be symmetric, $J_c(x) = J_c(-x)$. Using an asymmetric form would typically lead to a critical current which shows node lifting – the minima of $I_c(B)$ have nonzero values. While this feature is present in the measured critical current, it can be accounted for by factors other than an asymmetric current distribution,[2] such as relatively small aspect ratios ($\sim$5), and a non-sinusoidal current-phase relationship arising from a large junction transparency. Using a symmetric $J_c$ avoids this ambiguity, and has the additional advantage of providing a more direct comparison between our method and that of Dynes and Fulton.

The likelihood function is maximized by allowing the $A_n$ coefficients to vary at each Monte Carlo step. As $N$ is increased the posterior distribution of the current density widens, an indication of over-fitting. This increase in uncertainty serves as a criterion for choosing $N$, which for the typical dataset is between 4 and 8. The priors of $A_n$ are set to the uniform distribution $[-\max(I_c), \max(I_c)]$.

An example of our method is shown in Fig. S2, using $N = 5$. The current density is peaked at the edges of the sample, a feature also recovered in the DF approach. The corresponding critical current is in good agreement with the measured one, with the exception of the regions close to the nodes. Fig. S2 indicates that the supercurrent through the junction flows mainly along its edges. As a further test of the edge state contribution, we modify the functional form of the current density in Eq. (49), to explicitly allow for edge states. We add delta functions to the current density at the edges of the sample, $J_c(x) \to J_c(x) + d_L\delta(x + W/2) + d_R\delta(x - W/2)$, and estimate the contribution of edge states as the ratio of $d_L + d_R$ to the total current density $J_c^{\mathrm{tot}}$. As the carrier density approaches zero a significant fraction of the supercurrent is carried by the edge states, with $(d_L + d_R)/J_c^{\mathrm{tot}} \simeq 0.45$

(see Fig. S3).

The amount of disorder leading to the appearance of guided edge modes in our samples can indeed be expected to be different at the two edges. However, as shown earlier in the Supplementary Information, the mean free path of the guided edge modes is estimated to be significantly larger than the junction length. This is a consequence of weak confinement at the edge, making the edge mode wavefunctions extend far from the edge and lie mostly outside of the confining potential. Such states can diffract around disorder at the edge gaining large mean free path. As a result, impurity scattering is ineffective, so we expect a similar amount of current flowing at the two edges, and use a theoretical model where symmetry is explicitly built in.

Current asymmetry generically leads to interference patterns which show node lifting, a phenomenon where the minima of the critical current $I_c(B)$ acquire non-zero values. Because minimal node lifting is observed experimentally, the distributions are qualitatively expected to be almost symmetric. This behavior provides indirect confirmation of the guided edge mode model, which allows for a large degree of symmetry even in the presence of disordered edges. While minor node lifting is present in the measured data, it can be ascribed to other factors than an asymmetric current distribution, such as a large aspect ratio, and non-sinusoidal current phase relations. The use of a symmetric current model avoids the ambiguity of which combinations of factors lead to node lifting.

To give bounds on asymmetry of edge currents, we include results on Bayesian analysis for non-symmetric distributions. The effect of an asymmetric current distribution can be quantified by adding $\sum_{i=1}^{N} B_n \sin(2\pi nx/L)$ to the current distribution $J_c(x)$, with N=5 as for the symmetric part. We have included a new figure (Fig. S4) showing the spatial distribution of current through the junction, which remains peaked at the edges but becomes slightly asymmetric as a consequence of node-lifting.

Normal state device characterization

We have provided normal state characteristics of the graphene layer in Fig. S6 and used conventional wisdom to determine whether devices are clean, including Dirac point width and Fabry-Perot oscillations, both of which indicate high quality flakes. To assess the intrinsic graphene quality, we estimate the charge inhomogeneity to be in the low $10^{10}$ $cm^{-2}$ range based on Dirac point width on the normal resistance curves. Note that this is a conservative upper bound that likely overestimates the amount of disorder because the presence of Fabry-Perot resonances on the hole side broadens the curve (Fig. S6). By comparison, the edge-dominated transport regime exists over a widow extending to densities $\sim 2 - 3 \times 10^{11}$ $cm^{-2}$ (see Fig. 2d; also Figs. 3a, 4a of the main text) away from the charge neutrality point, exceeding the intrinsic charge inhomogeneity by roughly an order of magnitude. Furthermore, the window (in density) of edge-dominated transport consistently exceeds the charge inhomogeneity in multiple devices that exhibit edge currents (see caption of Fig. S6 for detailed parameters).

As a second indicator of quality, the existence of Fabry-Perot interferences on the hole side of normal state resistance curves show that the samples are in the ballistic limit (see Fig. S6). Large spatial density fluctuations would prevent such resonances from being resolved in transport. Edge currents only appear in the cleanest devices and tend to emerge in ballistic samples that exhibit Fabry-Perot interference, which suggests that the observed edge states are indeed correlated with higher sample quality. The reproducibility of the width of the edge currents over many independent samples also

rules out random disorder effects, which would yield a wide range of edge peak shapes and widths. While current annealing has been noted to enhance quality, it is not strictly necessary for observation of edge modes, which have been observed in both annealed and non-annealed devices.

We estimate the contact quality as follows: at carrier density $n = 10^{11} \ cm^{-2}$, the normal state resistance of device ML1 is 350 Ohms (Fig. S6a). At this density, the Fermi wavelength is $\lambda = 112$ nm. Given that the width of the device is W=1200 nm, the number of conducting channels (N) can be estimated from the sample geometry using the relation $N = aW/(\lambda/2) = 84$ modes, where $a = 4$ accounts for the spin and sublattice degeneracies in graphene. The ideal conductance is therefore $84e^2/h = 307$ Ohms. By comparing this value to the measured resistance, this yields a total estimated contact resistance of 43 Ohms, or transmission coefficient of $\sim 90\%$.

<div align="center">REFERENCES</div>

[1] A. Patil, D. Huard, and C. J. Fonnesbeck (2010). Pymc: Bayesian stochastic modelling in python. *Journal of statistical software*, 35(4):1

[2] J. P. Heida, B. J. van Wees, T. M. Klapwijk, and G. Borghs, Phys. Rev. B **57**, R5618(R) (1998).

## Supplementary Tables

| Device | L (nm) | W (nm) | Aspect ratio, L/W | Contact width (nm) |
|--------|--------|--------|-------------------|--------------------|
| BL1 | 250 | 1200 | 0.208 | 400 |
| ML1 | 300 | 1200 | 0.25 | 300 |
| BL2 | 300 | 800 | 0.375 | 400 |
| BL3 | 350 | 1200 | 0.292 | 600 |
| BL4 | 250 | 900 | 0.278 | 400 |

TABLE 1. List of device dimensions for the graphene Josephson junctions studied in this work. $L$ and $W$ refer to junction length and width, respectively, as labeled in Fig. 1d of the main text. Contact width refers to the size of the superconducting Ti/Al electrodes in the direction perpendicular to W. BLx and MLx refer to bilayer and monolayer graphene devices, respectively.

## Supplementary Figures
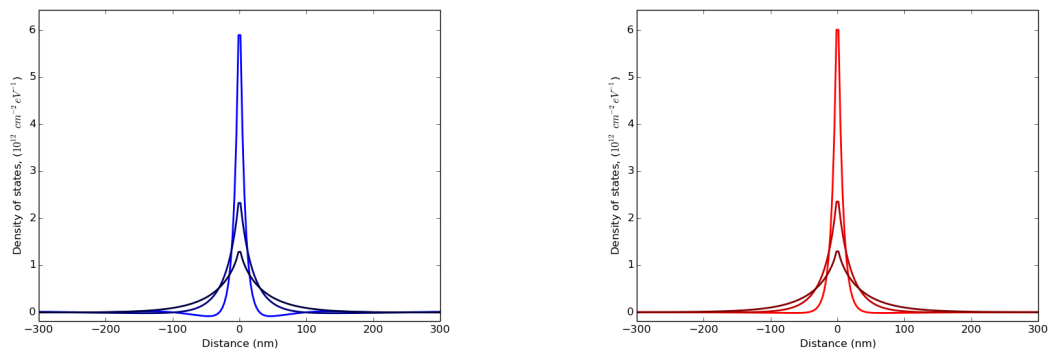


FIGURE S1. **Spatially-resolved density of states (DOS) for guided modes in MLG obtained for a delta-function line potential model.** Plotted is the excess contribution to the spatially-resolved DOS, $\Delta N(\varepsilon, x) = N(\varepsilon, x) - N_0(\varepsilon)$ vs. distance from the delta function, where we subtracted the bulk contribution $N_0(\varepsilon)$ given in Eq. (7). The left panel shows the full excess contribution obtained from Eq. (8), the right panel shows the contribution solely due to the guided modes, Eq. (24). The two contributions are nearly identical, confirming that the peak in DOS can serve as a signature of the guided modes. Parameter values used: $\hbar u = -1.5\hbar v$, energies $\varepsilon = \varepsilon_0, 0.5\varepsilon_0, 0.1\varepsilon_0$, where $\varepsilon_0 = \pi\hbar\sqrt{\pi n_0}$, $n_0 = 10^{11}\,\mathrm{cm}^{-2}$ (higher peaks correspond to higher energy values $\varepsilon$).
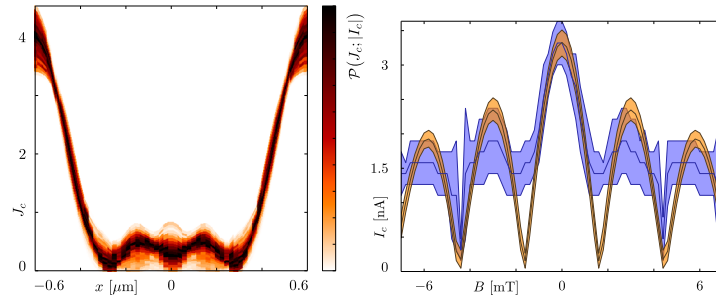
FIGURE S2. **Bayesian estimation method for extracting the current distribution.** Posterior distribution of the current density (left panel), and corresponding critical current (right panel). The values of $I_c$ obtained from the posterior distribution (orange) are in good agreement with the measured critical current (blue).
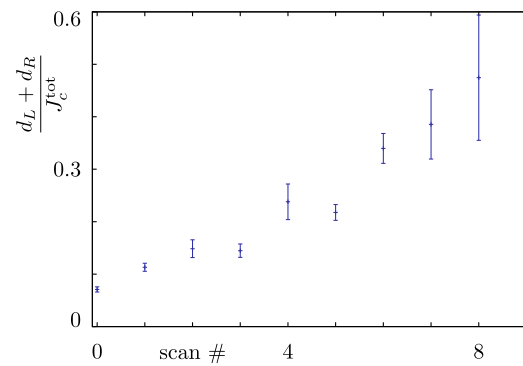


FIGURE S3. **Bayesian estimation results: ratio of the supercurrent carried by the edge states as a function of carrier density.** Each scan corresponds to a Fraunhofer pattern, with Fig. S2 showing the $8^{\text{th}}$ scan. (Increasing scan number corresponds to decreasing carrier density.)
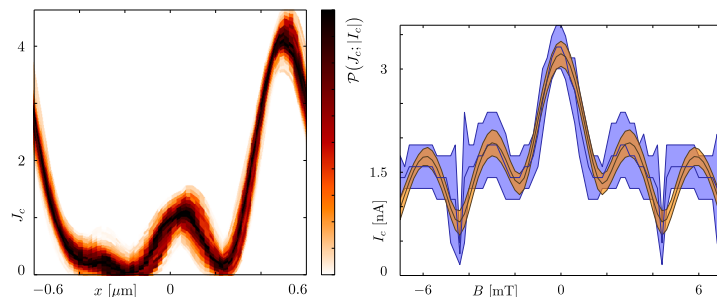
FIGURE S4. **Bayesian method for extraction of asymmetric current distributions.** Same as Fig. S2, but including the effect of an asymmetric current distribution by adding $\sum_{i=1}^{N} B_n \sin(2\pi n x/L)$ to the current distribution $J_c(x)$, with $N = 5$ as for the symmetric part. The posterior current density distribution (left) remains peaked at the edges, but becomes asymmetric, as a consequence of node-lifting. The corresponding critical current is now in good agreement with the measured one also in the node regions (right).
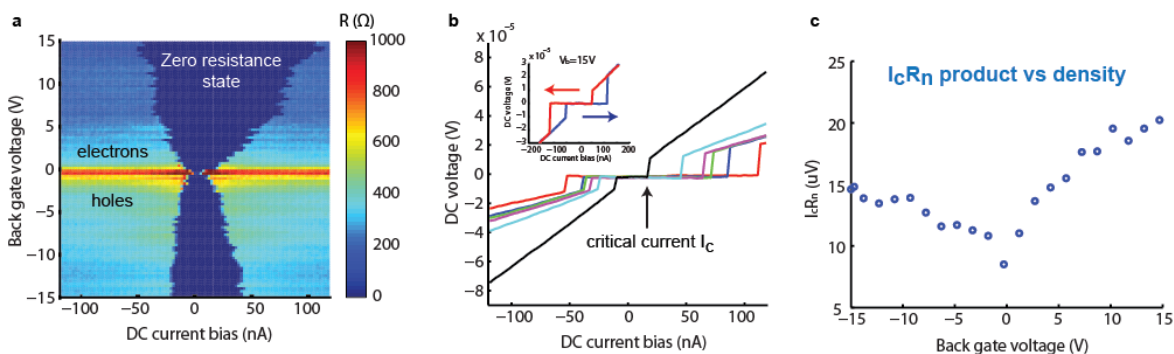


FIGURE S5. **Characterization of proximity induced superconductivity in a bilayer graphene Josephson junction.** **(a)** Bipolar supercurrent in graphene, observed in a color map of resistance as a function of DC current bias and back gate voltage. The zero resistance superconducting state is indicated in dark blue, while the normal state resistance is indicated by the colored regions at high bias. **(b)** I-V curves from the data in part (a), plotted for various fixed densities. A DC current bias is applied between the electrodes, and the resulting voltage drop across the junction is recorded. The critical current $I_c$ marks the transition between dissipationless and resistive states. The inset shows typical hysteresis curves based on scan direction of the applied current bias. **(c)** Plot of the $I_c R_n$ product for the data in part (a), where $I_c$ is the critical current and $R_n$ is the normal state resistance. Suppression is observed near the Dirac point, consistent with previous observations in graphene Josephson junctions.
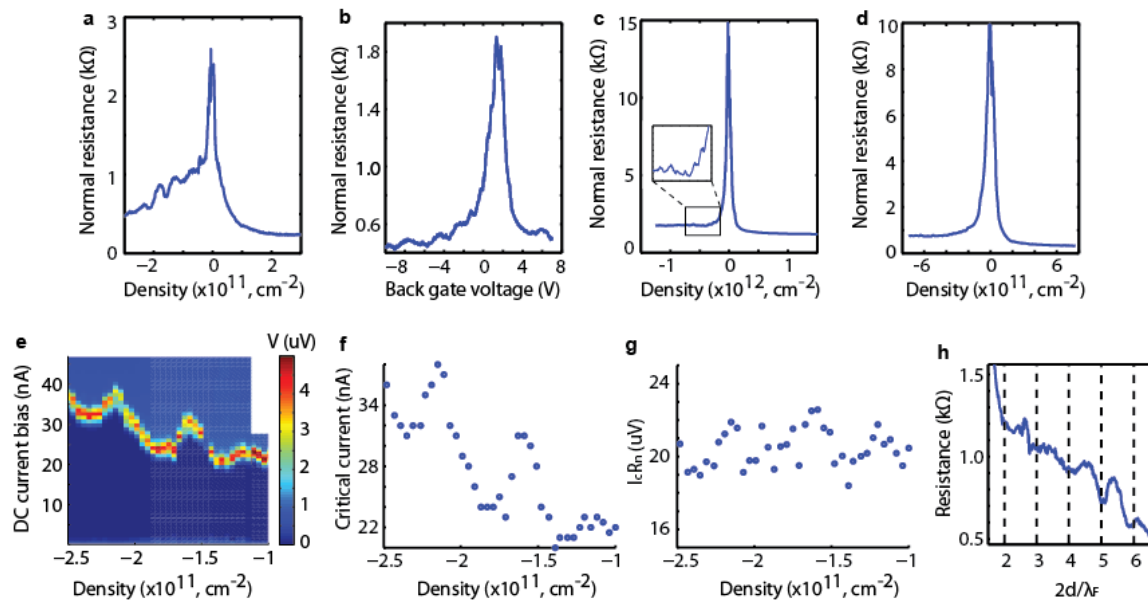
FIGURE S6. **Normal resistance characterization and ballistic supercurrent propagation in graphene Josephson junctions.** **(a)** Normal resistance of device ML1. At hole dopings, Fabry-Perot oscillations appear, a signature of ballistic transport. The Dirac point's full width at half maximum is about $3.4 \times 10^{10}\,\mathrm{cm}^{-2}$. The edge-to-bulk crossover density is roughly $3 \times 10^{11}\,\mathrm{cm}^{-2}$. **(b)** Normal resistance of device BL4. Ballistic Fabry-Perot oscillations also appear on the hole side. **(c)** Normal resistance of device BL2. Signatures of Fabry-Perot interference appear upon zooming into the hole side of the neutrality point (see inset). The Dirac point's full width at half maximum is about $6.9 \times 10^{10}\,\mathrm{cm}^{-2}$. The edge-to-bulk crossover density is roughly $-3 \times 10^{11}\,\mathrm{cm}^{-2}$. **(d)** Normal resistance of device BL3. The Dirac point's full width at half maximum is about $8 \times 10^{10}\,\mathrm{cm}^{-2}$. The edge-to-bulk crossover density is roughly $-2.5 \times 10^{11}\,\mathrm{cm}^{-2}$. **(e)** Ballistic supercurrent oscillations in the Fabry-Perot regime, shown in a plot of applied DC current bias vs density at zero magnetic field. The critical current $I_c$ marks the transition between dissipationless and resistive states. Data taken from device ML1. **(f)** Plot of critical current $I_c$ oscillations from the data in panel (e). **(g)** Plot of the $I_c R_n$ product from the data in panel (e). **(h)** Oscillations in panel (a) plotted versus $2d/\lambda_F$, where $\lambda_F$ is the Fermi wavelength and $d = 225$ nm is the effective cavity length. Resonances appear when the constructive interference conditions are satisfied for electron waves in a resonator, $2d = N\lambda_F$ for integer $N$, verifying that the oscillations are indeed associated with Fabry-Perot interference.
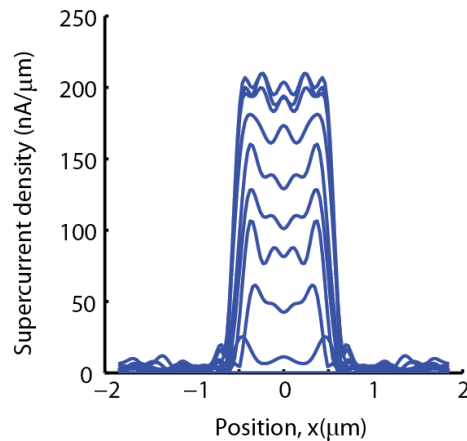
FIGURE S7. **Additional superconducting interferometry plots for device ML1, showing edge to bulk transition in real space over a large range of carrier density.** Supercurrent density distribution as a function of position, for the carrier density range $\sim 0 - 7 \times 10^{11}$ cm$^{-2}$, corresponding to the data in Fig. 2d of the main text.
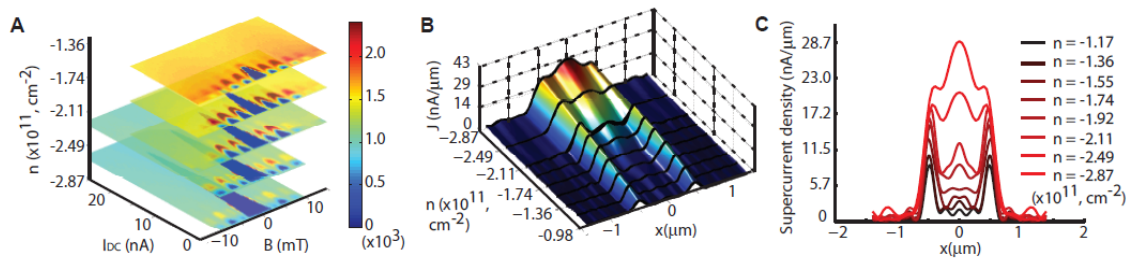


FIGURE S8. **Additional superconducting interferometry plots for device BL3.** **(A)** Sequence of Fraunhofer measurements in bilayer device $BL3$ for the current maps in panels (B) and (C), shown in plots of $dV/dI(\Omega)$ as a function of magnetic field $B$ (mT) and current bias $I_{DC}$ (nA). **(B)** Real space image of current flow $J(x)$ as a function of carrier density on the hole side, showing edge currents near the Dirac point and a continuous evolution of bulk flow. **(C)** Individual line cuts of $J(x)$ plotted from (B). This is the data set in Fig. 4a of the main text, plotted with a properly scaled vertical axis (supercurrent density, nA/$\mu$m).